# Molecular Insights into the Complex Relationship between Capacitance and Pore Morphology in Nanoporous Carbon-based Supercapacitors

Alexander J. Pak and Gyeong S. Hwang*

McKetta Department of Chemical Engineering, University of Texas, Austin, Texas 78712, United States

**S** *Supporting Information*

**ABSTRACT:** Electrochemical double layer capacitors, or super-capacitors, are high-power energy storage devices that consist of large surface area electrodes (filled with electrolyte) to accommodate ion packing in accordance with classical electric double layer (EDL) theory. Nanoporous carbons (NPCs) have recently emerged as a class of electrode materials with the potential to dramatically improve the capacitance of these devices by leveraging ion confinement. However, the molecular mechanisms underlying such enhancements are a clear departure from EDL theory and remain an open question. In this paper, we present the concept of ion reorganization kinetics during charge/discharge cycles, especially within highly confining subnanometer pores, which necessarily dictates the capacitance. Our molecular dynamics voltammetric simulations of ionic liquid immersed in NPC electrodes (of varying pore size distributions) demonstrate that the most efficient ion migration, and thereby largest capacitance, is facilitated by nonuniformity of shape (e.g., from cylindrical to slitlike) along nanopore channels. On the basis of this understanding, we propose that a new structural descriptor, coined as the pore shape factor, can provide a new avenue for materials optimization. These findings also present a framework to understand and evaluate ion migration kinetics within charged nanoporous materials.
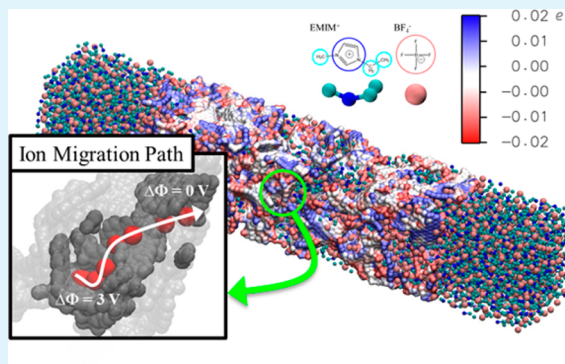
**KEYWORDS:** *pore size factor, subnanometer confinement, ionic liquid, molecular dynamics, constant potential, ion migration kinetics*

## INTRODUCTION

Providing energy access to the continuously growing global population demands critical developments in energy storage technologies. For example, efficient energy storage can mend the disconnect, and associated inefficiencies, between the energy supplied by power plants and intermittent alternative energy sources (e.g., solar and wind) and the energy demanded by consumers using the electric grid.[1,2] In addition, compact energy storage that is both gravimetrically and volumetrically efficient is also a necessity as mobile devices, electric vehicles, and other portable electronics become increasingly ubiquitous.[3,4] This has motivated the exploration of many types of energy storage technologies, including mechanical, chemical, thermal, and electrochemical. Among these, electrochemical energy storage (EES) is perhaps the most prevalent.[5] Within this space, lithium ion batteries have been one of the most popular EES technologies owing to their large energy densities. The emergence of high-power applications, however, diminishes the appeal of batteries due to sluggish charge-transfer kinetics limiting their power densities. An alternate stand-alone or hybrid EES solution is offered through electrochemical double layer capacitors (EDLCs), or supercapacitors, which are known for their large power densities and long lifetimes.[3,5,6] Yet compared to batteries, the energy density of EDLCs tends to be

at least an order of magnitude smaller. As such, many research efforts have been dedicated toward improving the characteristically low energy density of these devices.

Supercapacitors operate through formation of the so-called electric double layer, in which injected charge carriers are compensated by the accumulation of electrolyte ions at the electrode—electrolyte interface. The resultant energy density ($E$) is determined by the capacitance $C$ and the applied voltage $V$ such that $E = \frac{1}{2}CV^2$ in the linear response regime, or more generally, $E = \int C(V)V \, dV$. Efforts to improve $E$ have focused on finding new materials for both the electrode and electrolyte. For example, ionic liquids, which are solvent-free ions that remain in the liquid phase at room temperature, have the potential to replace traditional aqueous and organic electrolytes due to their excellent electrochemical stability, which can allow larger operating voltages up to 4 V.[7,8] Additionally, the search for new electrode materials has been directed toward improving $C$, which historically[9−11] has been by increasing the specific surface area ($S$) in accordance with double-layer theory[12,13] as referred in the original Standard Oil Company of Ohio patent[14]

of 1966. As such, carbon nanomaterials have been explored as replacements to commercially used activated carbons.

Most recently, the research community has shifted toward optimizing electrode materials by controlling the average pore size, which was motivated by experimental observations of enhanced $C$ once pores were small enough to accommodate only single ions.[15−17] This presents a new direction, beyond maximizing $S$, to dramatically improve $C$. However, the influence of pore size on $C$ remains a subject of debate due to several contradictory experimental results.[18,19] One potential source of this experimental inconsistency is the common practice of reporting $C$ normalized to the measured specific surface area ($S$), or the so-called areal capacitance, which is highly sensitive to the characterization method used.[18] Interestingly, when $C$ is normalized to the more reliably measured electrode mass, or the so-called specific (or gravimetric) capacitance, a clear dependence on pore size can be absent.[20] Another issue brought forth by a series of theoretical studies, which simulated confined ions within nanoslits, is that the optimal areal $C$ tends to vary with both pore size and applied potential.[21−25] These previous works have implied that the aforementioned experimental discrepancies may be attributed to different pore size dispersity throughout the electrode structure,[21−24] which might also indirectly influence the capacitance through pore-width-dependent dielectric screening.[25] Therefore, it would be worthwhile to understand the exact relationship between pore size dispersity and both areal and specific $C$.

In this article, we approach the study of $C$ in nanoporous materials through a different perspective, in which we relate $C$ to the kinetics of ion reorganization within the nanoporous electrode. This is motivated by the inherently dynamic and rapid operation of supercapacitor devices. Our study consists of 1-ethyl-3-methylimidazolium (EMIM) tetrafluoroborate (BF$_4$) ionic liquid (IL) confined within morphologically disordered nanoporous carbon (NPC) electrodes by classical molecular dynamics (MD). Here, we limit ourselves to NPCs consisting primarily of near-subnanometer pores to explore the effects of extreme ion confinement. In addition, we consider only pure IL electrolyte, which removes potential complexity due to solvation effects. Our analysis, which relies on our simulated voltammetric process, demonstrates that the efficiency of charge carrier storage and utilization depends on the ability of counterions to migrate, especially from within highly confining pores. We identify a possible molecular mechanism for ion extraction, and on the basis of this understanding, we relate, for the first time, the (integral) areal and specific capacitances of different NPC electrodes (with varying pore sizes and pore size dispersity) to a new unified structural descriptor coined as the pore shape factor (PSF), which can be easily quantified via common experimental characterization techniques.

## RESULTS

**Simulation Framework.** As depicted in Figure 1, our simulation consists of a two-electrode EDLC cell with EMIM$^+$BF$_4^-$ IL electrolyte, which is modeled with a coarse-grained force field (see Computational Methods). NPC electrodes were generated to ensure sp$^2$ hybridization with hydrogen-passivated edges (see Computational Methods), which are hereafter denoted as NPC-12A, NPC-10A, and NPC-9A, in accordance with each of their average pore sizes. Table 1 summarizes their structural properties (specific surface
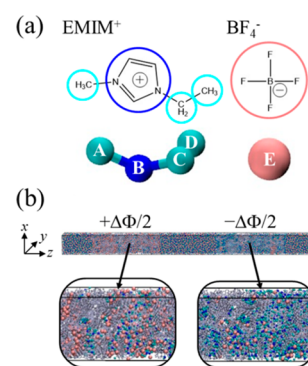


**Figure 1.** (a) Schematic of the EMIM/BF$_4$ ionic liquid studied in this work. Each ion is coarse-grained such that a group of atoms (circled) is modeled as a single interaction site. In particular, the EMIM$^+$ cation is modeled with four interaction centers (shown by the cyan and blue spheres labeled A−D) while the BF$_4^-$ anion is modeled with a single interaction center (shown by the pink sphere labeled E). (b) Schematic of the simulation domain (periodic in all three directions) consisting of two 16 nm porous carbon electrodes (shown by gray lines) immersed in ionic liquid (shown by the cyan, blue, and pink spheres). The length of the simulation domain is 60 nm in the $z$ direction. The left (right) electrode is positively (negatively) polarized with total applied potential $\Delta\Phi$.

**Table 1. Summary of Structural Characteristics of the Three Nanoporous Carbon Electrodes Studied in This Work[a]**

|  | NPC-12A | NPC-10A | NPC-9A |
|---|---|---|---|
| density $\rho$, g/cm$^3$ | 0.96 | 1.03 | 1.09 |
| surface area $S$, m$^2$/g | 1072 | 836 | 750 |
| pore volume $V_p$, cm$^3$/g | 0.185 | 0.121 | 0.093 |
| average pore size $W_p$, Å | 12.4 | 10.8 | 9.6 |
| hydrogen content, at. % | 8 | 10 | 11 |

[a]Structural characteristics were determined with a spherical probe with a comparable adsorption cross-section to N$_2$ (∼2.25 Å). All pore geometry analysis was performed via a Monte Carlo sampling approach described in ref 26. Specific surface areas and pore volumes computed with different gas molecule probes can be found in Figure S1.

area, pore volume, and average pore size), as characterized by a Monte Carlo sampling technique;[26] additional information is provided, such as their mass densities and hydrogen contents. We should note that these properties are based on spherical sampling probes with a radius of 2.25 Å to emulate adsorption by N$_2$ molecules; results based on different probe radii are shown in Figure S1. In each simulation, the charge equilibration scheme[27] (see Computational Methods) is adapted to emulate constant potential surfaces with an imposed potential difference ($\Delta\Phi = \Phi_{pos} - \Phi_{neg}$) with reference to the surface potentials of the positive and negative electrodes.

We first study the case of NPC-9A electrodes when neutral and charged, in order to clarify the connection between the distribution of electrolyte ions and electrode surface charge. We then emulate a discharge cycle, similar to cyclic voltammetry, using nonequilibrium MD in which $\Delta\Phi$ is linearly modulated over time. Our analysis focuses on the resultant redistribution of electrolyte ions and electrode charges. Finally, we evaluate and compare the (integral) capacitances for each of the three electrodes, which have varying average pore width. Our findings demonstrate that the areal and specific capacitances are strongly dependent on kinetic factors, namely, the efficiency of ion migration and reorganization; on the basis of this under-

standing, we propose that materials design of electrodes should focus on a new physical descriptor introduced in this work, termed the pore shape factor (PSF), rather than the recently explored pore width.

**Relationship between Electrolyte Ion and Electrode Charge Redistribution.** In this section, we analyze the organization of electrolyte ions throughout the nanoporous electrodes in relation to the electrode charge redistribution. The benefit of our simulation-based approach is the ability to probe molecular-scale phenomena, which we leverage to show the existence of significant nanoscale inhomogeneity of both the electrode charge and ion distribution while, macroscopically, the electrodes remain at a constant applied potential.

To clarify this phenomenon, we adopt the degree of confinement (DoC) definition as described in ref 28. to characterize the types of electrode surfaces that ions contact, hereafter referred to as contact sites, at different polarizations. Briefly, the DoC is related to the coordination number of an ion with its nearest-neighbor electrode atoms (e.g., within 6.2 Å as determined from radial distribution functions) and quantifies the fraction of the solid angle around an ion that is occupied by electrode atoms.[28] We distinguish five separate types of sites including edges (DoC < 16%), planes (16% < DoC < 37%), hollows (37% < DoC < 60%), pockets (DoC > 60%), and other (DoC = 0%). The first four sites are depicted in the snapshots shown in Figure 2, while the "other" qualification refers to the portion of the electrode that has only co-ions or no ions in its vicinity. Note that these definitions are based on natural partitions throughout the DoC profiles depicted in Figure 2; here, the maximum DoC defined for each site tends to be slightly larger than those of ref 28, as our electrode structures incorporate hydrogen-terminated edges.

First, let us consider when $\Delta\Phi$ is held at 0 V (the total corresponding charge of each electrode is less than 1 C/g) The fractional distributions of all cations and anions as a function of DoC are depicted in Figure 2a,b. The largest fraction of both cations and anions can be found at the planar sites (16−37% DoC); here, the availability of space allows the cations and anions to be well-mixed, as seen in the depicted snapshot, in order to maintain local charge neutrality. Correspondingly, the electrode surface at the planar sites exhibits minimal charge polarization, as evidenced by the nearly null electrode charge ($\sigma_{elec}$) shown in Figure 2c,d; here, we have chosen to represent $\sigma_{elec}$ as the sum of partial charges of the local electrode atoms normalized to the DoC, which essentially serves as a proxy for the average partial charge per atom. Beyond the planar sites, smaller fractions of both cations and anions are located within the hollow and pocket sites. Interestingly, we find that the magnitude of $\sigma_{elec}$ adjacent to cations (anions) at these sites (Figure S2) is slightly larger than that of the planar sites while the negative (positive) sign of $\sigma_{elec}$ indicates that these sites exhibit electron accumulation (depletion). This suggests that electrode charge inhomogeneity is induced to compensate for a local imbalance in ionic charge, which can especially occur in confined regions as the limited volume restricts spatially uniform mixing of cations and anions.

Upon charging the electrodes and holding $\Delta\Phi$ at 3 V, a redistribution of both electrode charge and electrolyte ions throughout the porous electrode is clearly observed. Yet, similar to the neutral case, the local electrode and ionic charge are found to be inherently connected. For example, counterions tend to migrate from planar sites toward hollow and pocket sites, as evidenced by the shift toward larger DoC in the
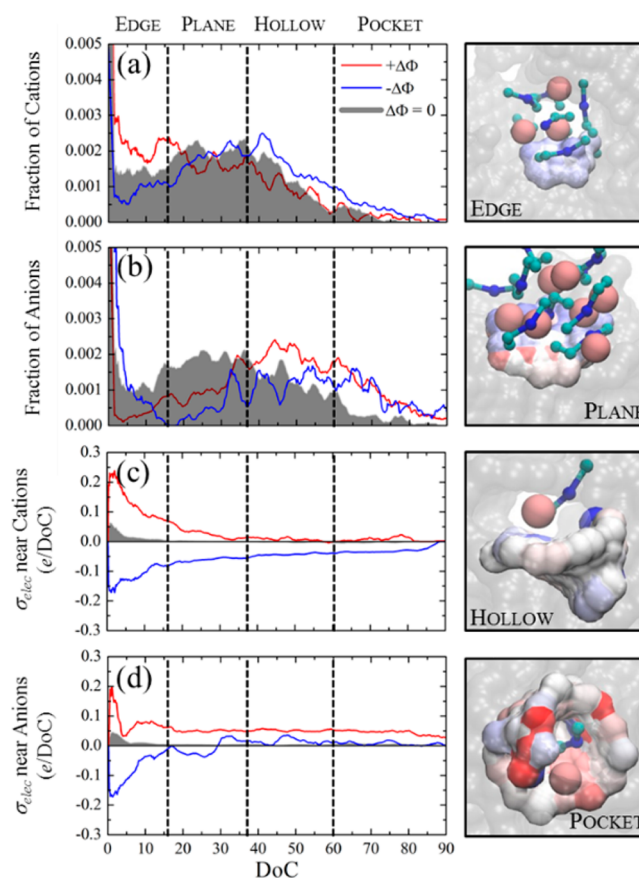


**Figure 2.** (a, b) Fractional distribution of (a) cation and (b) anion degrees of confinement (DoC, %) within the NPC-9A electrode when the full-cell applied potential ($\Delta\Phi$) is 0 and 3 V. (c, d) Electrode charge normalized by DoC ($\sigma_{elec}$) of adjacent (c) cation and (d) anion when $\Delta\Phi$ = 0 and 3 V as a function of DoC. Dashed lines depict the boundaries that distinguish edge, plane, hollow, and pocket sites. The four snapshots on the right represent each of the four sites; colored surface contours depict electrode atoms with color corresponding to charge [from −0.1e (red) to +0.1e (blue)], pink spheres depict the $BF_4^-$ anion, and blue and cyan ball-and-sticks depict the $EMIM^+$ cation, while transparent surface contours represent other electrode atoms. All snapshots were rendered with VMD.[29]

distribution profiles of $EMIM^+$ (Figure 2a) and $BF_4^-$ (Figure 2b), since single ions can more effectively screen the distributed electrode charge once confined. Yet interestingly, the magnitude of $\sigma_{elec}$ adjacent to the counterions (Figure 2c,d) tends to slightly diminish with increasing DoC, which suggests that the electrode charge polarization is more broadly (or spatially) distributed in confined regions.

The size of the constituent ions also influences both the ion and electrode charge redistribution. Consider that the charge of an $EMIM^+$ cation is more spatially distributed than that of a $BF_4^-$ anion due to their bulky and compact sizes, respectively. As a result, the electrode is more weakly polarized by $EMIM^+$ compared to $BF_4^-$, which is reflected by the smaller magnitude of $\sigma_{elec}$ near $EMIM^+$ counterions. The compact nature of $BF_4^-$ has another consequence in that $BF_4^-$ co-ions are observed in pocket sites (Figure 2b) even when the electrodes are negatively charged; to accommodate the anion, the local pocket electrode atoms tend to be electron-depleted (Figure 2d). We should note that this observed charge inhomogeneity due to the local ionic environment is possible only when the electrode material is metallic and easily polarizable.
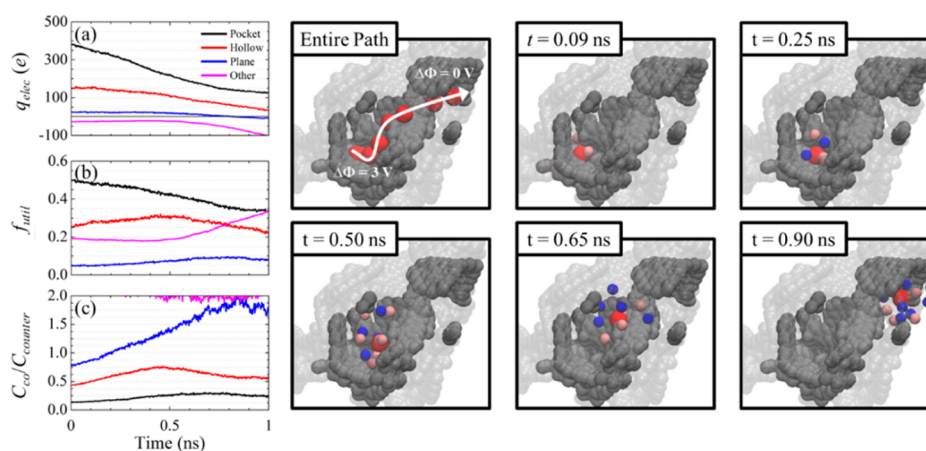
**Figure 3.** Discharge profiles of the positive NPC-9A electrode when the applied full-cell potential varies from 3 to 0 V over 1 ns in a nonequilibrium MD simulation. (a) Excess charge stored per listed counterion adsorption site ($q_{elec}$) as a function of time. (b) Atomic fraction of the electrode utilized ($f_{util}$) as each listed site as a function of time. (c) Ratio of anion–cation coordination number ($C_{co}$) to anion–anion coordination number ($C_{counter}$) at the listed site as a function of time. Snapshots on the right depict the path of a counterion that begins in a pocket site and ends detached from the surface. The electrode is depicted as the gray (transparent) surface within 6 Å (15 Å) of the counterion, while the counterion is depicted as a solid red sphere. Adjacent $BF_4^-$ anions and $EMIM^+$ cations within 6 Å of the tracked counterion are depicted as pink and blue spheres, respectively. For clarity, only the imidazolium interaction center of $EMIM^+$ is shown. All snapshots were rendered with VMD.[29]

We should also mention that chemical functionalization of the electrode material can impact charge heterogeneity along the electrode surface, although perhaps to a lesser degree. Consider the peak seen in the $\sigma_{elec}$ profiles (Figure 2c,d) when DoC < 5%. This DoC region corresponds to positively charged hydrogen atoms that terminate the electrode edges, which explains the large magnitude of $\sigma_{elec}$ relative to the other DoC regions. In addition, it is well-known that injected charge carriers preferentially accumulate at edge carbon atoms,[30] which we also observe as demonstrated by the relatively larger increase of $\sigma_{elec}$ at the edge sites once the electrodes are charged (Figure 2d). Nonetheless, our focus will be on the other contact sites (i.e., planes, hollows, and pockets), as the edge sites contribute only a small portion toward capacitive storage given their relatively low atomic concentration (~10 at. %).

Finally, we briefly compare these insights to that of Merlet et al.,[28] who previously studied a NPC electrode immersed in an IL electrolyte. These researchers attributed the large capacitance for NPC electrodes to a greater amount of total local charge stored at contact sites with increasing DoC at a fixed $\Delta\Phi$.[28] However, as discussed above, it is also important to normalize this charge with respect to the DoC, similar to $\sigma_{elec}$ used in this work, in order to approximate the stored charge per electrode atom, which essentially indicates the specific capacitance ($C_{sp}$). In fact, our analysis demonstrates that $\sigma_{elec}$ decreases with increasing DoC, which suggests that contact sites contribute less to $C_{sp}$ as their DoC increases. However, the contribution of each type of contact site to the areal capacitance ($C_{ar}$) is more difficult to quantify and should depend upon the change in specific surface area of each contact site as the DoC increases.

**Relationship between Capacitance and Extraction of Confined Ions/Excess Charge.** In most experimental studies of EDLCs, the capacitance is quantified through dynamical processes such as cyclic voltammetry or galvanostatic charge–discharge cycles. We emulate a similar process by initially precycling our two-electrode NPC-9A system (see Computational Methods) before analyzing the electrode charge and ion reorganization over a 1 ns discharge. In this section, we will

demonstrate that the integral capacitance is strongly dependent on the kinetics of counterion migration from highly confined contact sites toward minimally confined contact sites during discharge.

As $\Delta\Phi$ decreases from 3 to 0 V, the total excess charge of the electrode ($q_{elec}$) decreases from 214.8 to 7.6 C/g for a specific discharge capacitance ($C_{sp} = 2\Delta q_{elec}/m\Delta\Phi$) of 138 F/g or areal capacitance ($C_{ar} = 2\Delta q_{elec}/S\Delta\Phi$) of 18 $\mu F/cm^2$; we should clarify that the factor of 2 is adopted to emulate the common experimental approximation for the half-cell potential used for symmetric two-electrode cells. It is notable that $q_{elec}$ does not deplete to null charge upon complete discharge, as the implication is that excess charge carriers remain trapped. Given the aforementioned relationship between local electrode charge and adjacent ions, this further implies that ions do not fully transition from the segregated state (described in the charged case above) to the well-mixed state (described in the neutral case above) and instead populate an intermediary quasi-equilibrium state. To clarify this behavior, we next explore the capacitive contributions of the pocket, hollow, and planar counterion contact sites; here, only the positive electrode is shown for simplicity.

In Figure 3a, $q_{elec}$ values of the pocket, hollow, and planar sites are depicted during the discharge process; note that the categorization of each electrode atom as a particular contact site is recomputed throughout the simulation as the local ionic environment also changes. Interestingly, after discharge, we find that $q_{elec}$ values of the pocket and hollow sites far exceed that of the total electrode. In other words, these sites remain $BF_4^-$ counterion-rich such that the local electrode surface is significantly electron-depleted in order to balance the total local charge. Throughout the rest of the electrode, in particular at the "other" adsorption sites, which can be $EMIM^+$ co-ion-rich, the aforementioned depleted electron density is compensated such that the total $q_{elec}$ is reduced toward null charge. In this discharged state, the electrode surface charge is nonuniformly distributed as cations and anions remain fairly segregated, which suggests that the transition toward a well-

mixed cation/anion state under null potential can be hindered by kinetic barriers.

To understand the kinetic limitations of discharge, we investigate the mechanism of $BF_4^-$ counterion extraction from pocket sites during discharge. We consider two aspects of the counterion contact to the electrode surface—(1) the atomic fraction of the electrode utilized as each contact site ($f_{util}$) and (2) the ratio of the anion−cation to anion−anion nearest-neighbor coordination numbers ($C_{co}/C_{counter}$)—to elucidate the composition of ions surrounding the contacted counterion. In Figure 3b, we make an interesting observation. While $f_{util}$ values of the pocket and planar sites expectedly decrease and increase, respectively, that of the hollow sites varies nonmonotonically, initially increasing before decreasing during discharge. This behavior suggests that the hollow sites may be involved as a transition site to facilitate ion extraction from pocket sites. This is especially counterintuitive as the $q_{elec}$ of the hollow sites monotonically decreases (Figure 3a) while counterions increasingly migrate toward hollow sites, which suggests that the electrostatic attraction between the electrode wall and counterions is not the dominant driving force for this behavior.

The $C_{co}/C_{counter}$ profiles, shown in Figure 3c, provide an important hint to explain this behavior. In particular, we find that $C_{co}/C_{counter}$ of the hollow sites has a bell-shaped profile similar to that of the $f_{util}$ profile shown in Figure 3b. The initial increase in $C_{co}/C_{counter}$ implies that neighboring ions reorganize such that $EMIM^+$ co-ions constitute a greater fraction of the ions that surround the counterion in contact with the electrode surface. The electrostatic attraction between counterions and co-ions can compensate for the locally depleting $q_{elec}$ throughout the hollow sites in order to stabilize counterion accumulation; without the presence of co-ions to compensate the ionic charge, the extraction of electrode charge can be unfavorable. Eventually, once $q_{elec}$ has sufficiently depleted, counterions (and their coordinated co-ions) tend to migrate from hollow sites to increasingly less confined sites, as reflected by the decreasing $f_{util}$ and $C_{co}/C_{counter}$ values of the hollow sites. The molecular snapshots presented in Figure 3 depict a representative example of this process, where a counterion gradually migrates along the electrode surface from a pocket site toward a pore cavity (i.e., a void large enough to contain a bulklike electrolyte region) with commensurate ion reorganization around it.

**Relationship between Pore Structure, Ion Extraction Efficiency, and Discharge Capacitance.** On the basis of the presented understanding of electrode charge and ion extraction during discharge, we now evaluate and compare the discharge capacitances of three different NPC electrodes with varying average pore width ($W_p$). In this section, we introduce a structural feature termed PSF (pore shape factor) that relates capacitance to electrode structure in a more complete fashion than $W_p$.

Figure 4 shows the computed $C_{ar}$ (Figure 4a) and $C_{sp}$ (Figure 4b) for the three NPC electrodes with average $W_p$ varying from around 12 to 9 Å at different $\Delta\Phi$. First, $C_{ar}$ exhibits a clear correlation to $W_p$; specifically, with $\Delta\Phi = 3$ V, $C_{ar}$ is predicted to increase from 13 to 18 $\mu F/cm^2$ as $W_p$ decreases from around 12 to 9 Å. However, we should note that the relative improvement in $C_{ar}$ based on $W_p$ strongly depends upon the approximated value of the specific surface area (Figure S3). Indeed, the work of Centeno and co-workers[18,19] recently highlighted that experimentally reported trends relating $C_{ar}$ to $W_p$ could qualitatively change depending on the use of
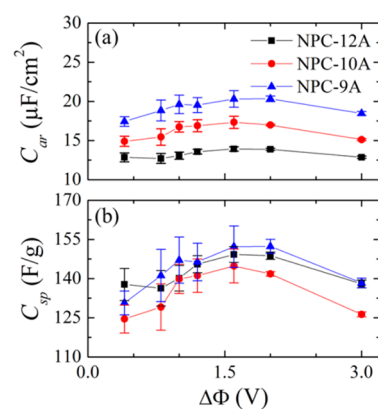


**Figure 4.** Comparison of (a) areal ($C_{ar}$) and (b) specific ($C_{sp}$) discharge capacitances as a function of applied full-cell potential ($\Delta\Phi$) for each nanoporous carbon electrode in a two-electrode configuration immersed in $EMIM/BF_4$ ionic liquid. The capacitances were calculated from the specific surface area (based on a $N_2$ gas probe) or mass of a single electrode. Note that the differences between computed $C_{ar}$ can vary significantly depending on the choice of gas molecule for structural characterization (Figure S3). Here, we do not consider the electrode capacitance contribution, as it is assumed to be much larger than the double-layer contribution due to the presence of edge and topological defects.

Brunauer−Emmett−Teller (BET) surface areas compared to other independent techniques.

In many ways, $C_{sp}$ is a more reliable performance metric than $C_{ar}$, as the electrode mass is much easier to measure reliably than $S$; note that for actual devices (i.e., including packaging, active materials, and separators), volumetric capacitances might be the most reliable benchmark.[31] Yet, as seen in Figure 4b, the aforementioned trend with $W_p$ is not predicted to translate to comparable trends in $C_{sp}$; the NPC-9A and NPC-12A electrodes are estimated to have the largest $C_{sp}$ (around 138 F/g at $\Delta\Phi = 3$ V). Therefore, a different physical descriptor of the electrode morphology, especially one that is consistent with both $C_{ar}$ and $C_{sp}$, can be a powerful guide for future electrode design. Given our previous analysis of ion and electrode charge redistribution during discharge, it is apt to investigate the differences between the three electrodes along this direction.

Figure 5a,b shows the $f_{util}$ profiles of the pocket and hollow sites, respectively, during discharge. A notable difference among the three cases is observed in pocket site utilization. Specifically, the NPC-12A and NPC-9A cases, which also have the largest $C_{sp}$, exhibit the greatest change in $f_{util}$ of the pocket sites. This behavior is commensurate with greater uptake of hollow site $f_{util}$ (Figure 5b) (and $C_{co}/C_{counter}$ as seen in Figure S4) during the initial phase of discharge. In addition, since the initial $f_{util}$ values of the pocket sites are comparable in all three electrode cases, a greater change in $f_{util}$ indicates more efficient counterion extraction from the pocket sites. Furthermore, this suggests that the capacitive contribution from pocket sites with more efficient ion extraction is also larger on an atomic/mass basis (further analysis described in Figure S5). Therefore, the current evidence points to $C_{sp}$ being strongly correlated with the efficacy of counterion removal from confined sites.

In order for the necessary reorganization of ions along the electrode surface to occur, the pore network should consist of pore channels with smoothly varying shape (e.g., from cylindrical to planarlike) and/or curvature. We propose that one way to approximate the pore shape, if we assume that the
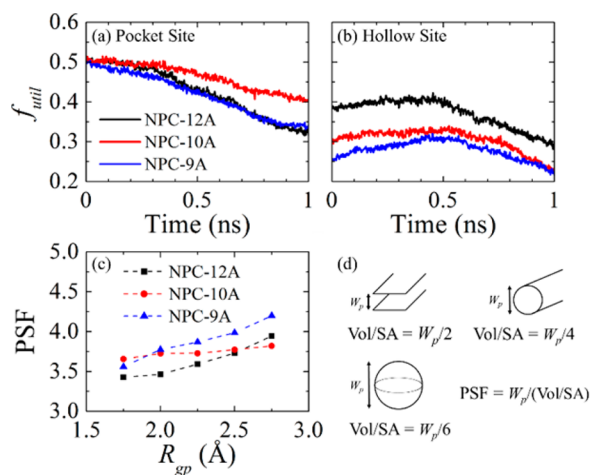
**Figure 5.** Discharge profiles for each of the nanoporous carbon (NPC) electrodes at the positive terminal when the applied full-cell potential is linearly varied from 3 to 0 V over 1 ns in a nonequilibrium MD simulation. The fraction of the electrode utilized ($f_{util}$) as a (a) pocket and (b) hollow site as a function of time is plotted. In addition, (c) the PSF (pore shape factor) of each electrode as a function of the gas probe radius ($R_{gp}$) used to measure the surface area and pore volume is shown. (d) Schematic depicting the PSF of different types of pores.

majority of the electrode consists of negative-curvature surfaces, is through knowledge of $S$, $W_p$, and pore volume ($V_p$). Then we define the aforementioned PSF:

$$\text{PSF} = \frac{W_p}{\left(\dfrac{V_p}{S/2}\right)}$$

such that the pores are mostly slitlike when PSF = 2, cylindrical-like when PSF = 4, and spherical-like when PSF = 6 (see Figure 5d); as we are primarily concerned with the shape of the region ions experience under confinement, we consider only the inner surface area of the negative curvature surfaces, which is approximated with the additional factor of $^1/_2$. The dispersity (i.e., nonuniformity) of PSF can then be qualitatively assessed by the change in PSF with respect to the radius of the probe molecule ($R_{gp}$) used to measure $S$ and $V_p$ ($\approx \partial \text{PSF}/\partial R_{gp}$). Figure 5c shows the calculated PSF with varying $R_{gp}$ for each NPC electrode. The larger positive slope seen in the NPC-12A and NPC-9A cases compared to the NPC-10A case indirectly confirms that the former two electrodes have greater pore shape dispersity, that is, variable shape along nonuniform nanopore channels, and therefore more efficient ion reorganization and larger $C_{sp}$.

**Applicability of the Pore Shape Factor: Comparison with Experiments.** The PSF can also be helpful to understand trends in $C_{ar}$. Consider that the effective surface area per electrode atom in cylindrical pocket sites can be reduced compared to surfaces with less curvature (e.g., planar sites). Since $C_{ar}$ and $C_{sp}$ are related by $S$ ($C_{ar} = C_{sp}/S$), a smaller $S$ can result in larger $C_{ar}$. Hence, if we consider the PSF when $R_{gp} = 2.25$ Å (e.g., $N_2$), we find that our predicted $C_{ar}$ increases as PSF increases and approaches 4 (i.e., cylindrical-like); here, it is important to consider PSFs based on a pore distribution that (i) primarily consists of ion-accessible pores and (ii) is consistent with $S$. We can also extend this analysis to previously reported experimental capacitances ($C$) of nanoporous carbon.

In Figure 6a, we compare $C$ as a function of PSF from six different experimental sources. Here, the BET surface area
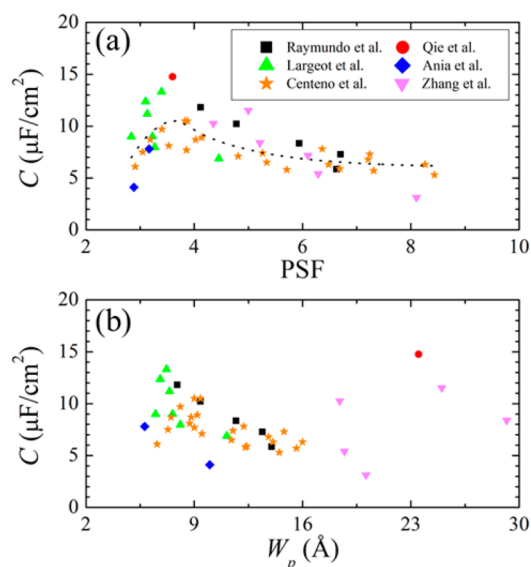


**Figure 6.** Comparison of experimental areal capacitance ($C$) based on BET surface areas with respect to (a) pore shape factor (PSF) and (b) pore width ($W_p$). The dashed line in panel a serves as a visual guide. All experimental data were obtained from refs 16, 18, and 32−35.

(using $N_2$) is used and the $W_p$ is estimated from provided pore size distributions when not directly reported;[36] note that the PSF may also be useful to check consistency with the underlying shape kernel used to characterize the pore size distributions, surface areas, or pore volumes. Remarkably, a distinct correlation is observed, with the maximum appearing to be centered around PSF ≈ 3.7, which is close to idealized cylindrical-like pores. In this case, the maximum PSF may be around 4, as this shape best favors the contact area between ions and the electrode surface; it is possible that the optimal PSF is sensitive to the shape and size of the ions. In comparison, $C$ as a function of $W_p$ is presented in Figure 6b. The correlation with $W_p$ is much weaker, which is consistent with the work of Centeno and co-workers[18,19] that showed a nearly independent relationship between $C$ and $W_p$. This suggests that the areal capacitance may be described more consistently by the pore shape, characterized as PSF in this work, rather than by $W_p$. However, in materials with very narrow pore size distributions (e.g., carbide-derived carbons or CDCs), a strong correlation with $W_p$ may still be present.

## ■ SUMMARY

We investigated the relationship between the structural properties of nanoporous carbons (immersed in EMIM/BF$_4$ ionic liquid) and the discharge capacitance by classical molecular dynamics with a coarse-grained force field and a fluctuating charge method to simulate constant-potential electrodes. The three electrodes studied in this work had average pore widths of 12.4, 10.8, and 9.6 Å with large specific capacitances ($C_{sp}$, normalized to mass) of 138, 126, and 138 F/g, respectively, and areal capacitances ($C_{ar}$, normalized to surface area) of 13, 15, and 18 $\mu$F/cm$^2$, respectively, at 3 V; we should note that we implicitly assume that the electrode (quantum) capacitance contribution is negligible, as even a small fraction (<2 at.%) of edges and topological defects can dramatically increase the availability of electronic states near the charge neutrality point.[30,37] We analyzed the molecular origin of these capacitance values by specifically studying redistrib-

ution of both the electrode charge and electrolyte ions during discharge. Our results show that significant charge can remain trapped within sites in which counterions are highly confined by the electrode surface. Counterion extraction was found to require electrode topologies with pore channels of smoothly variable size and shape, which in turn facilitated the reorganization of neighboring ions that allowed counterions to migrate from confined sites toward pore cavities containing bulklike electrolyte regions. One implication of this work is that a larger $C_{sp}$ is associated with more efficient counterion extraction. In addition, a larger $C_{ar}$ was attributed to pore shapes that, on average, maximize the contact between ions and the electrode surface. Therefore, a new structural property was proposed, termed the pore shape factor (PSF), which was demonstrated to show a strong correlation to experimental data. This simple metric can serve as the basis of an alternative physical descriptor (for example, variation of PSF with respect to the size of the probe molecule) to unify commonly used characterizations, including pore width, specific surface area, and pore volume.

These findings suggest that the design of future materials for supercapacitors requires an understanding of the relationship between pore size/shape dispersity and the molecular migration and reorganization of ions (and charge carriers) under dynamic conditions. We anticipate that such insights may also help resolve observed anomalies in impedance measurements[38] and improve phenomenological transmission line models,[39,40] which are commonly used to describe impedance and capacitance. For example, future studies of ion reorganization rates near different types of contact sites may elucidate characteristic time scales based on morphological features and ion geometry. In addition, the approach presented in this work can be extended to study additional factors, including the presence of chemical impurities/functional groups,[41,42] solvation effects,[43] and dependencies on charging/discharging rate.[44,45] In principle, the working model can be refined to incorporate electrolyte polarization at the electrode interface[46] and possible nonlinear screening throughout the NPC.[47] Finally, these results highlight the importance of reporting in-depth experimental characterization of the electrode structure, including pore size distributions, specific surface areas, and pore volumes, using different gas adsorbates, which can be used to estimate the PSF. The PSF (and its dispersity) may prove to be a useful guide to accelerate the design and discovery of nanoporous carbons for high-performance supercapacitors.

## ■ COMPUTATIONAL METHODS

**Electrode Structure Generation.** Initial NPC structures were generated by use of the Mimetic model presented in ref 48. Simulation domains were $4.55 \times 4.55 \times 20$ nm$^3$ (using periodic boundary conditions) with initial number densities of 0.05, 0.054, and 0.06 Å$^{-3}$ in a face-centered cubic (fcc) lattice configuration. Temperatures were quenched from 20 000 to 700 K under the NVT ensemble by use of the Nosé−Hoover thermostat[49] with a quench time of 1.6 ns and time step of 0.07 fs. After generation, 2 nm of carbon atoms was removed from each end to make the structures nonperiodic in the $z$ direction. Then unphysical and dangling carbons were removed from the system, after which hydrogen atoms were attached to the remaining sp carbon. The volumes were then relaxed in the $xy$ direction under the NPT ensemble by use of a Nosé−Hoover barostat/thermostat[49] and AIREBO potential[50] for 500 ps with a time step of 1 fs. The final $xy$ dimensions of NPC-12, NPC-10, and NPC-9 electrodes were $4.54 \times 4.54$, $4.57 \times 4.57$, and $4.58 \times 4.58$ nm$^2$, respectively.

**Force Field.** The ionic liquid was described by use of a coarse-grained approach such that EMIM$^+$ and BF$_4^-$ were reduced to four and one interaction centers, respectively, as depicted in Figure 1. The nonbonding parameters were adapted from ref 51 as summarized in Table 2; the charges ($q$) were rescaled following the fashion of ref 52,

**Table 2. Coarse-Grained Parameters**[a]

| site | $\varepsilon$ (kcal/mol) | $\sigma$ (Å) | $q$ (e) |
|------|-----|------|------|
| A | 0.157 | 3.90 | 0.1733 |
| B | 0.643 | 4.32 | 0.3741 |
| C | 0.141 | 3.90 | 0.1647 |
| D | 0.157 | 3.90 | 0.0679 |
| E | 0.339 | 4.1 | −0.7800 |

[a]Parameters are primarily from refs 51 and 53, with $q$ rescaled following the fashion of ref 52 and $\sigma$ reoptimized to reproduce experimental density and diffusivity.

while the zero-energy pairwise distances ($\sigma$) were reoptimized to reproduce experimental density and diffusivity. The bond, angle, and dihedral parameters were adopted from ref 53, with the latter case adapted for the OPLS form. The Lennard-Jones (LJ) parameters for electrode carbon and hydrogen atoms were taken from ref 54. All LJ and Coulomb energies were calculated by use of a spherical cutoff radius of 16 Å, with long-range Coulomb energies included by the particle−particle particle-mesh method.[55]

The charge of each electrode atom was allowed to fluctuate to emulate constant-potential surfaces (with ΔΦ). We adapted the charge equilibration[27] (Qeq) scheme, based on electronegativity equalization, which is commonly used in ReaxFF simulations.[56] Here, the electronegativity of the positive (negative) electrode is rigidly shifted by -ΔΦ/2 (+ΔΦ/2) and the charges are solved iteratively with the sum of the total electrode charge constrained to zero. The short-range Coulomb interactions included shielding corrections,[56] while the long-range Coulomb interactions were solved by the fast multipole method.[57] The Qeq parameters for carbon and hydrogen were adopted from ref 58.

**Molecular Dynamics Simulations.** All MD simulations were performed by use of LAMMPS[59] and consisted of two fixed 16 nm electrodes separated by 14 nm of electrolyte, as seen in Figure 1, for a total length of 60 nm in the $z$ direction with periodic boundary conditions in all three directions; the cross-sectional areas were consistent with that of each electrode. Each simulation was initially sparse with a $z$ length of 90 nm and 4164 IL pairs that were randomly distributed outside the electrodes. Initial equilibration was run for 10 ns under the NVT ensemble with a temperature of 850 K controlled by a Nosé−Hoover thermostat with a 1 ps damping factor and 2 fs time step. During this period, the electrode atoms were kept rigid with null charge and moved linearly to their final positions; the simulation domain was also linearly deformed to its final length. A second equilibration step was performed at ΔΦ = 0 V for 10 ns with the electrode charges updated every 100 fs and the temperature gradually decreased from 850 to 300 K. With the temperature fixed at 300 K, charges were updated every 2 fs while the systems were further equilibrated over 1 ns. Similarly, a ΔΦ = 3 V was impulsively applied and equilibrated for 2 ns. Finally, molecular trajectories were extracted every 5 ps over a production run of 4 ns to compute the DoC profiles.

To prepare the capacitance calculations, each simulation underwent precycling by linearly varying ΔΦ between 0 and the target ΔΦ for at least three charge and two discharge ramps with 1 ns in each direction (total precycling time was at least 5 ns); the precycling was considered complete when the largest and smallest peak-to-peak values of the electrode charge deviated by less than 1% from the previous cycle. Discharge production runs were carried out by first holding ΔΦ for 250 ps before allowing ΔΦ to linearly decrease to 0 V over 1 ns; molecular trajectories were extracted every 2 ps.

All reported results were extracted from the average trajectories from four independent simulations with different initial atomic

configurations. Additional details on the analysis of trajectories can be found in Supporting Information.

## ASSOCIATED CONTENT

### Supporting Information

The Supporting Information is available free of charge on the ACS Publications website at DOI: 10.1021/acsami.6b11192.

Five figures depicting specific surface area and pore volume of nanoporous carbons using different gas probe radii, DoC-normalized electrode charge with neutral potential, areal capacitance normalized to different surface areas, and extra analysis of ion migration/ reorganization and charge redistribution kinetics during discharge (PDF)

## AUTHOR INFORMATION

### Corresponding Author

*E-mail gshwang@che.utexas.edu.

### ORCID

Gyeong S. Hwang: 0000-0002-5538-9426

### Notes

The authors declare no competing financial interest.

## ACKNOWLEDGMENTS

## REFERENCES

(1) Barton, J. P.; Infield, D. G. Energy Storage and Its Use with Intermittent Renewable Energy. *IEEE Trans. Energy Convers.* **2004**, *19*, 441−448.

(2) Yang, Z.; Zhang, J.; Kintner-Meyer, M. C. W.; Lu, X.; Choi, D.; Lemmon, J. P.; Liu, J. Electrochemical Energy Storage for Green Grid. *Chem. Rev.* **2011**, *111*, 3577−3613.

(3) Chen, H.; Cong, T. N.; Yang, W.; Tan, C.; Li, Y.; Ding, Y. Progress in Electrical Energy Storage System: A Critical Review. *Prog. Nat. Sci.* **2009**, *19*, 291−312.

(4) Karden, E.; Ploumen, S.; Fricke, B.; Miller, T.; Snyder, K. Energy Storage Devices for Future Hybrid Electric Vehicles. *J. Power Sources* **2007**, *168*, 2−11.

(5) Winter, M.; Brodd, R. J. What Are Batteries, Fuel Cells, and Supercapacitors? *Chem. Rev.* **2004**, *104*, 4245−4269.

(6) Yu, G.; Xie, X.; Pan, L.; Bao, Z.; Cui, Y. Hybrid Nanostructured Materials for High-Performance Electrochemical Capacitors. *Nano Energy* **2013**, *2*, 213−234.

(7) Armand, M.; Endres, F.; MacFarlane, D. R.; Ohno, H.; Scrosati, B. Ionic-Liquid Materials for the Electrochemical Challenges of the Future. *Nat. Mater.* **2009**, *8*, 621−629.

(8) Van Aken, K. L.; Beidaghi, M.; Gogotsi, Y. Formulation of Ionic-Liquid Electrolyte to Expand the Voltage Window of Supercapacitors. *Angew. Chem., Int. Ed.* **2015**, *54*, 4806−4809.

(9) Morimoto, T.; Hiratsuka, K.; Sanada, Y.; Kurihara, K. Electric Double-Layer Capacitor Using Organic Electrolyte. *J. Power Sources* **1996**, *60*, 239−247.

(10) Simon, P.; Gogotsi, Y. Capacitive Energy Storage in Nanostructured Carbon-Electrolyte Systems. *Acc. Chem. Res.* **2013**, *46*, 1094−1103.

(11) Jiang, H.; Lee, P. S.; Li, C. 3D Carbon Based Nanostructures for Advanced Supercapacitors. *Energy Environ. Sci.* **2013**, *6*, 41−53.

(12) Helmholtz, H. Ueber Einige Gesetze Der Vertheilung Elektrischer Ströme in Körperlichen Leitern Mit Anwendung Auf Die Thierisch-Elektrischen Versuche. *Ann. Phys.* **1853**, *165*, 211−233.

(13) Stern-Hamburg, O. Zur Theorie der elektrolytischen Doppelschicht. *Z. Elektrochem. Angew. Phys. Chem.* **1924**, *30*, 508−516.

(14) Rightmire, R. A. Electrical Energy Storage Apparatus. U.S. Patent US 3288641 A, November 29, 1966

(15) Chmiola, J.; Yushin, G.; Gogotsi, Y.; Portet, C.; Simon, P.; Taberna, P. L. Anomalous Increase in Carbon Capacitance at Pore Sizes Less than 1 Nanometer. *Science* **2006**, *313*, 1760−1763.

(16) Largeot, C.; Portet, C.; Chmiola, J.; Taberna, P.; Gogotsi, Y.; Simon, P. Relation between the Ion Size and Pore Size for an Electric Double-Layer Capacitor. *J. Am. Chem. Soc.* **2008**, *130*, 2730−2731.

(17) Galhena, D. T. L.; Bayer, B. C.; Hofmann, S.; Amaratunga, G. A. J. Understanding Capacitance Variation in Sub-Nanometer Pores by In-Situ Tuning of Interlayer Constrictions. *ACS Nano* **2016**, *10*, 747−754.

(18) Centeno, T. A.; Sereda, O.; Stoeckli, F. Capacitance in Carbon Pores of 0.7 to 15 nm: A Regular Pattern. *Phys. Chem. Chem. Phys.* **2011**, *13*, 12403−12406.

(19) Stoeckli, F.; Centeno, T. A. Pore Size Distribution and Capacitance in Microporous Carbons. *Phys. Chem. Chem. Phys.* **2012**, *14*, 11589−11591.

(20) Zuliani, J. E.; Tong, S.; Kirk, D. W.; Jia, C. Q. Isolating the Effect of Pore Size Distribution on Electrochemical Double-Layer Capacitance Using Activated Fluid Coke. *J. Power Sources* **2015**, *300*, 190−198.

(21) Feng, G.; Cummings, P. T. Supercapacitor Capacitance Exhibits Oscillatory Behavior as a Function of Nanopore Size. *J. Phys. Chem. Lett.* **2011**, *2*, 2859−2864.

(22) Jiang, D. E.; Jin, Z.; Wu, J. Oscillation of Capacitance inside Nanopores. *Nano Lett.* **2011**, *11*, 5373−5377.

(23) Xing, L.; Vatamanu, J.; Borodin, O.; Bedrov, D. On the Atomistic Nature of Capacitance Enhancement Generated by Ionic Liquid Electrolyte Confined in Subnanometer Pores. *J. Phys. Chem. Lett.* **2013**, *4*, 132−140.

(24) Kondrat, S.; Pérez, C. R.; Presser, V.; Gogotsi, Y.; Kornyshev, A. A. Effect of Pore Size and Its Dispersity on the Energy Storage in Nanoporous Supercapacitors. *Energy Environ. Sci.* **2012**, *5*, 6474.

(25) Kondrat, S.; Kornyshev, A.; Stoeckli, F.; Centeno, T. A. The Effect of Dielectric Permittivity on the Capacitance of Nanoporous Electrodes. *Electrochem. Commun.* **2013**, *34*, 348−350.

(26) Willems, T. F.; Rycroft, C. H.; Kazi, M.; Meza, J. C.; Haranczyk, M. Algorithms and Tools for High-Throughput Geometry-Based Analysis of Crystalline Porous Materials. *Microporous Mesoporous Mater.* **2012**, *149*, 134−141.

(27) Rappe, A. K.; Goddard, W. A., III Charge Equilibration for Molecular Dynamics Simulations. *J. Phys. Chem.* **1991**, *95*, 3358−3363.

(28) Merlet, C.; Péan, C.; Rotenberg, B.; Madden, P. A.; Daffos, B.; Taberna, P.-L.; Simon, P.; Salanne, M. Highly Confined Ions Store Charge More Efficiently in Supercapacitors. *Nat. Commun.* **2013**, *4*, No. 2701.

(29) Humphrey, W.; Dalke, A.; Schulten, K. VMD: Visual Molecular Dynamics. *J. Mol. Graphics* **1996**, *14*, 33−38.

(30) Pak, A. J.; Paek, E.; Hwang, G. S. Impact of Graphene Edges on Enhancing the Performance of Electrochemical Double Layer Capacitors. *J. Phys. Chem. C* **2014**, *118*, 21770−21777.

(31) Gogotsi, Y.; Simon, P. True Performance Metrics in Electrochemical Energy Storage. *Science* **2011**, *334*, 917−918.

(32) Raymundo-Piñero, E.; Kierzek, K.; Machnikowski, J.; Béguin, F. Relationship between the Nanoporous Texture of Activated Carbons and Their Capacitance Properties in Different Electrolytes. *Carbon* **2006**, *44*, 2498−2507.

(33) Qie, L.; Chen, W.; Xu, H.; Xiong, X.; Jiang, Y.; Zou, F.; Hu, X.; Xin, Y.; Zhang, Z.; Huang, Y. Synthesis of Functionalized 3D Hierarchical Porous Carbon for High-Performance Supercapacitors. *Energy Environ. Sci.* **2013**, *6*, 2497.

(34) Ania, C. O.; Pernak, J.; Stefaniak, F.; Raymundo-Piñero, E.; Béguin, F. Polarization-Induced Distortion of Ions in the Pores of Carbon Electrodes for Electrochemical Capacitors. *Carbon* **2009**, *47*, 3158−3166.

(35) Zhang, L.; Yang, X.; Zhang, F.; Long, G.; Zhang, T.; Leng, K.; Zhang, Y.; Huang, Y.; Ma, Y.; Zhang, M.; Chen, Y. Controlling the Effective Surface Area and Pore Size Distribution of sp2 Carbon

Materials and Their Impact on the Capacitance Performance of These Materials. *J. Am. Chem. Soc.* **2013**, *135*, 5921−5929.

(36) The selected experimental works were limited to those that used pure ionic liquid electrolyte or organic electrolyte in order to avoid possible pseudocapacitive influences.

(37) Pak, A. J.; Paek, E.; Hwang, G. S. Tailoring the Performance of Graphene-Based Supercapacitors Using Topological Defects: A Theoretical Assessment. *Carbon* **2014**, *68*, 734−741.

(38) Suss, M. E.; Baumann, T. F.; Worsley, M. A.; Rose, K. A.; Jaramillo, T. F.; Stadermann, M.; Santiago, J. G. Impedance-Based Study of Capacitive Porous Carbon Electrodes with Hierarchical and Bimodal Porosity. *J. Power Sources* **2013**, *241*, 266−273.

(39) Barcia, O. E.; D'Elia, E.; Frateur, I.; Mattos, O. R.; Pébère, N.; Tribollet, B. Application of the Impedance Model of de Levie for the Characterization of Porous Electrodes. *Electrochim. Acta* **2002**, *47*, 2109−2116.

(40) Candy, J. P.; Fouilloux, P.; Keddam, M.; Takenouti, H. The Pore Texture of Raney-Nickel Determined by Impedance Measurements. *Electrochim. Acta* **1982**, *27*, 1585−1593.

(41) Pak, A. J.; Hwang, G. S. On the Importance of Regulating Hydroxyl Coverage on the Basal Plane of Graphene Oxide for Supercapacitors. *ChemElectroChem* **2016**, *3*, 741−748.

(42) Kerisit, S.; Schwenzer, B.; Vijayakumar, M. Effects of Oxygen-Containing Functional Groups on Supercapacitor Performance. *J. Phys. Chem. Lett.* **2014**, *5*, 2330−2334.

(43) Pean, C.; Daffos, B.; Rotenberg, B.; Levitz, P.; Haefele, M.; Taberna, P. L.; Simon, P.; Salanne, M. Confinement, Desolvation, and Electrosorption Effects on the Diffusion of Ions in Nanoporous Carbon Electrodes. *J. Am. Chem. Soc.* **2015**, *137*, 12627−12632.

(44) He, Y.; Huang, J.; Sumpter, B. G.; Kornyshev, A. A.; Qiao, R. Dynamic Charge Storage in Ionic Liquids-Filled Nanopores: Insight from a Computational Cyclic Voltammetry Study. *J. Phys. Chem. Lett.* **2015**, *6*, 22−30.

(45) Pak, A. J.; Hwang, G. S. Charging Rate Dependence of Ion Migration and Stagnation in Ionic Liquid-Filled Carbon Nanopores. *J. Phys. Chem. C* **2016**, *120*, 24560−24567.

(46) Sala, J.; Guàrdia, E.; Martí, J. Specific Ion Effects in Aqueous Eletrolyte Solutions Confined within Graphene Sheets at the Nanometric Scale. *Phys. Chem. Chem. Phys.* **2012**, *14*, 10799.

(47) Kuroda, M.; Tersoff, J.; Martyna, G. Nonlinear Screening in Multilayer Graphene Systems. *Phys. Rev. Lett.* **2011**, *106*, No. 116804.

(48) Shi, Y. A Mimetic Porous Carbon Model by Quench Molecular Dynamics Simulation. *J. Chem. Phys.* **2008**, *128*, No. 234707.

(49) Hoover, W. Canonical Dynamics: Equilibrium Phase-Space Distributions. *Phys. Rev. A: At., Mol., Opt. Phys.* **1985**, *31*, 1695−1697.

(50) Stuart, S. J.; Tutein, A. B.; Harrison, J. A. A Reactive Potential for Hydrocarbons with Intermolecular Interactions. *J. Chem. Phys.* **2000**, *112*, 6472.

(51) Daily, J. W.; Micci, M. M. Ionic Velocities in an Ionic Liquid under High Electric Fields Using All-Atom and Coarse-Grained Force Field Molecular Dynamics. *J. Chem. Phys.* **2009**, *131*, No. 094501.

(52) Roy, D.; Maroncelli, M. An Improved Four-Site Ionic Liquid Model. *J. Phys. Chem. B* **2010**, *114*, 12629−12631.

(53) Wang, Y.; Izvekov, S.; Yan, T.; Voth, G. A. Multiscale Coarse-Graining of Ionic Liquids. *J. Phys. Chem. B* **2006**, *110*, 3564−3575.

(54) Jorgensen, W. L.; Maxwell, D. S.; Tirado-rives, J. Development and Testing of the OPLS All-Atom Force Field on Conformational Energetics and Properties of Organic Liquids. *J. Am. Chem. Soc.* **1996**, *118*, 11225−11236.

(55) Toukmaji, A. Y.; Board, J. A. Ewald Summation Techniques in Perspective: A Survey. *Comput. Phys. Commun.* **1996**, *95*, 73−92.

(56) van Duin, A. C. T.; Dasgupta, S.; Lorant, F.; Goddard, W. A. ReaxFF: A Reactive Force Field for Hydrocarbons. *J. Phys. Chem. A* **2001**, *105*, 9396−9409.

(57) Nakano, A. Parallel Multilevel Preconditioned Conjugate-Gradient Approach to Variable-Charge Molecular Dynamics. *Comput. Phys. Commun.* **1997**, *104*, 59−69.

(58) Chenoweth, K.; van Duin, A. C. T.; Goddard, W. A. ReaxFF Reactive Force Field for Molecular Dynamics Simulations of Hydrocarbon Oxidation. *J. Phys. Chem. A* **2008**, *112*, 1040−1053.

(59) Plimpton, S. Fast Parallel Algorithms for Short-Range Molecular Dynamics. *J. Comput. Phys.* **1995**, *117*, 1−19.